applied sciences

MDPI

Article

Performance Evaluation of Planetary Boundary Layer Schemes in Simulating Structures of Wintertime Lower Troposphere in Seoul Using One-Hour Interval Radiosonde Observation

Beom-Soon Han [1], Kyung-Hwan Kwak [2,*], Jae-Hee Hahm [2,3] and Seung-Bu Park [4]

[1] Department of Environment and Energy, Semyung University, Jecheon 27136, Korea; bshan07@semyung.ac.kr
[2] School of Natural Resources and Environmental Science, Kangwon National University, Chuncheon 24341, Korea; jaehee3750@korea.kr
[3] National Typhoon Center, Korea Meteorological Administration, Seogwipo 63614, Korea
[4] School of Environmental Engineering, University of Seoul, Seoul 02504, Korea; sbpark3@uos.ac.kr
* Correspondence: khkwak@kangwon.ac.kr

Abstract: We investigated the structures of the wintertime lower troposphere in Seoul, South Korea on 17 and 18 January 2017 by performing 1 h interval radiosonde observation and numerical simulations. In the daytime on 17 January, the height of the convective boundary layer (CBL) sharply and quickly increased when the residual layer became a part of the CBL. From the afternoon on 17 January, moist air with clouds began to substantially intrude in the lower troposphere in Seoul, and radiative heating/cooling weakened. As a result, the mixing of air in the lower troposphere was inhibited and the vertical gradients of potential temperature and water vapor mixing ratio changed little on 18 January. We evaluated the performance of four planetary boundary layer (PBL) parameterization schemes (the Yonsei University (YSU), Mellor–Yamada–Janjić (MYJ), Mellor–Yamada–Nakanishi–Niino (MYNN), and Asymmetric Convective Model version 2 (ACM2) schemes) coupled with the Weather Research and Forecasting model in simulating the structures of the lower troposphere against 1 h interval radiosonde observation. The general tendencies of the air temperature and wind speed in the lower troposphere were well-reproduced in the four simulations. However, the sharp increase in the CBL height did not appear in the four simulations, implying that the process of the residual layer becoming a part of the CBL in the daytime is not well-parameterized. Additionally, the simulated water vapor mixing ratio near the surface was smaller compared with the observation. We found that small-scale turbulence in the CBL, which mixes advected air and pre-existing air, was not reproduced well by the PBL parameterization schemes. Compared with the other simulations, the most accurate air temperature and wind speed were reproduced in the simulation with the MYJ scheme, while the CBL development and moisture advection were reproduced relatively well in the simulation with the MYNN scheme.

Keywords: 1 h interval radiosonde observation; wintertime lower troposphere; WRF model; PBL scheme

Citation: Han, B.-S.; Kwak, K.-H.; Hahm, J.-H.; Park, S.-B. Performance Evaluation of Planetary Boundary Layer Schemes in Simulating Structures of Wintertime Lower Troposphere in Seoul Using One-Hour Interval Radiosonde Observation. *Appl. Sci.* **2022**, *12*, 6356. https://doi.org/10.3390/app12136356

Academic Editor: Harry D. Kambezidis

Received: 26 April 2022
Accepted: 19 June 2022
Published: 22 June 2022

1. Introduction

The structure of the lower troposphere is affected by many factors such as radiation, synoptic weather, and turbulent eddies. Solar radiation heats the surface and causes convection, which mixes air at different levels. Synoptic weather induces temperature or moisture advections, and dramatically changes the air temperature and water vapor mixing ratio in the lower troposphere. The turbulent eddies produced by surface forcing (e.g., surface heating and drag by topography) generate complicated wind patterns and mix the air. The changes in the lower troposphere directly affect humans near the surface; thus, many researchers have tried to reveal their nature through observation [1–4] and numerical simulation [5–8].

Observations of the lower troposphere using various instruments, such as radiosonde, radar, and lidar, have shown that the development of the convective boundary layer (CBL), one of the important processes in the lower troposphere, is variable and intricate in space and time. Cooper and Eichinger [9] observed the daytime lower troposphere and found that convective structures such as thermal plumes and convective eddies are produced by solar heating and play an important role in the development of the CBL. They also found that in the daytime lower troposphere, the upward transport of warm and polluted air near the surface is mainly governed by a spatially inhomogeneous process driven by convective structures. In addition to convective structures, the growth in the CBL is complex and affected by synoptic weather, land-use characteristics, local advection, land-sea contrast, and topography. For example, Bianco et al. [10] found that cold-air advection induced by sea breeze decreased air temperature and impeded the growth of the CBL. Ao et al. [11] observed that the development of the CBL in the lower troposphere was not always continuous and the CBL height could sharply increase when the residual layer became a part of the CBL. However, the time intervals of the abovementioned direct in situ observations were insufficient (i.e., typically larger than a 3 h interval) to capture such an abrupt change in the development of the CBL.

Numerical models have also been widely used to investigate the boundary layer structures in the lower troposphere. Because the length-scale of turbulence in the boundary layer is generally small, numerical models with a horizontal grid resolution larger than ~1 km use a planetary boundary layer (PBL) scheme, which parameterizes small-scale turbulence in the boundary layer based on observation, theory, and high-resolution simulation [12–14]. PBL schemes can successfully reproduce the general characteristics of boundary layer (e.g., air temperature, wind speed, and wind direction in boundary layer) [15–17]. However, detailed or abrupt changes in the CBL structures, such as convective structures, may not be reproduced by numerical simulations with PBL parameterization schemes.

The aforementioned studies commonly emphasize that the important CBL processes in the lower troposphere cannot easily be captured by operational in situ observations because of insufficient time interval nor reproduced by numerical models even incorporating typical PBL parameterization schemes, which motivates this study. In this study, we performed radiosonde observations with a 1 h interval on 17 and 18 January 2017 to intensively investigate abrupt changes in the CBL and lower troposphere in Seoul, South Korea. Additionally, we evaluated the performance of PBL schemes in simulating temporal changes in the structure of the lower troposphere through comparisons with the radiosonde observations. In Section 2, we analyze the synoptic weather conditions on 17 and 18 January 2017. In Section 3, we describe the radiosonde observation and simulation design. In Section 4, we present and discuss the radiosonde observation and simulation results. A summary and conclusions are given in Section 5.

2. Synoptic Weather Analysis

Figure 1 shows surface weather maps from the Korea Meteorological Administration (KMA) and horizontal wind vectors and water vapor mixing ratio at 900 hPa from the ERA5 data provided by the European Centre for Medium-Range Weather Forecasts (ECMWF) at 0900 LST on 17 and 18 January 2017. At 0900 LST on 17 January, the Korean Peninsula was influenced by a high-pressure system (Figure 1a). As a result, on the Korean Peninsula, the wind speed and water vapor mixing ratio were low (Figure 1c), which means the weather was calm and clear. These weather conditions were favorable for CBL development. On 18 January, a high-pressure system centered over the northern part of Korean Peninsula moved southeastward, so the influence of the high-pressure system on the Korean Peninsula weakened (Figure 1b). Additionally, westerly and northwesterly winds transported water vapor to the Korean Peninsula in the lower troposphere (Figure 1d). As a result, the weather became cloudy, and haze appeared during the nighttime on 17 and 18 January.

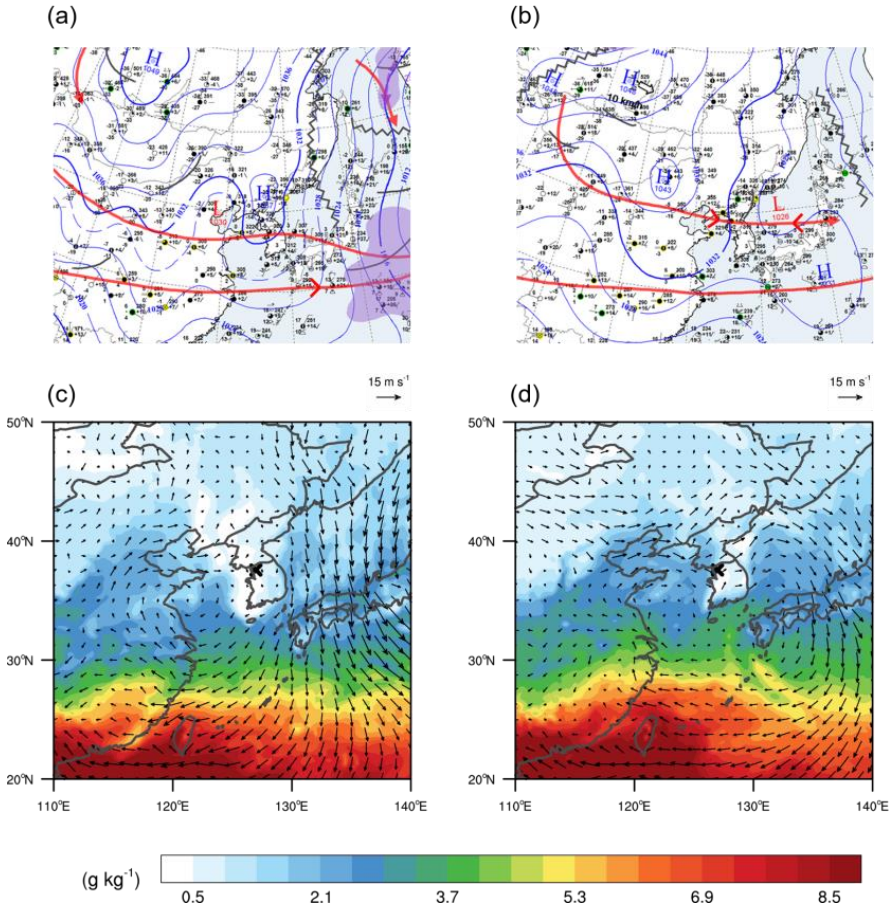

Figure 1. Surface weather maps at 0900 LST on (**a**) 17 and (**b**) 18 January 2017. Horizontal wind vectors and water vapor mixing ratio at 900 hPa at 0900 LST on (**c**) 17 and (**d**) 18 January 2017. The location of Seoul is indicated by the cross symbol. (**a**,**b**) L and H represent low- and high-pressure systems, respectively. Pressure trough and ridge in upper troposphere are indicated by the black straight and zigzag lines, respectively. Red lines and arrows represent jet streams in upper troposphere, and purple shaded areas represent jet streams in lower troposphere.

3. Data and Methods

3.1. Radiosonde and Ground Observation Data

To investigate the structures of the wintertime lower troposphere in an urban area, we performed an intensive observation using radiosondes (Jinyang RSG-20A) at Daemyeong Middle School, which was located in a central urban area of Seoul, South Korea (Figure 2). Jinyang RSG-20A has margins of error of 0.5 K, 1 hPa, and 5% for air temperature, air pressure, and relative humidity, respectively, which showed better performance with lower biases and errors compared with other operational radiosondes [4]. The observation period was from 2300 LST on 16 January to 0100 LST on 19 January 2017, and the radiosonde was launched every 1 h during the period. We launched a total of 51 radiosondes. We measured air pressure, air temperature, relative humidity, altitude of the radiosonde, wind speed, and wind direction, and the data acquisition interval was 1 s. From the observed air pressure, air temperature, and relative humidity, water vapor mixing ratio was diagnosed. We set short radiosonde launching and data acquisition intervals to precisely examine temporal variations in the lower troposphere in an urban area. Due to the short radiosonde launching interval (1 h), we halted the data acquisition from the radiosonde when the radiosonde reached a height of ~5 km. Discarding 4937 missing values, we used a total of 578,083 radiosonde observation values (99.1% of total) in this study.

Figure 2. Satellite image showing radiosonde-launching site and AWS site in Seoul (NAVER map).

To validate simulation results, we also used 2-m air temperature and 10-m wind speed observed at Gangnam Automatic Weather Station (AWS), which is located near the radiosonde launching site (Figure 2). The Gangnam AWS data were provided by the KMA. The AWS data recorded from 2300 LST on 16 January to 0100 LST on 19 January 2017 with the data interval of 1 h was used (i.e., 102 data points in total without any missing value).

3.2. Model and Simulation Design

To test the performance of the PBL parameterization schemes in simulating the wintertime lower troposphere in an urban area, we used Weather Research and Forecasting (WRF) model version 4.1.3 [18] in this study. We adopted four domains with two-way nesting, and the horizontal grid resolutions of the domains were 27, 9, 3, and 1 km (Figure 3). The model domain had 72 vertical layers and 43 vertical layers below ~2 km from the ground to accurately simulate the lower troposphere. The vertical grid resolution below 1.5 km was ~40 to ~50 m. We used the 6-hourly National Centers for Environmental Prediction (NCEP) final analysis data with a horizontal grid resolution of 0.25° as the initial and boundary conditions. We ran four simulations with the YSU [19], Mellor–Yamada–Janjić (MYJ, ref. [20]), Mellor–Yamada–Nakanishi–Niino (MYNN, ref. [21]), and Asymmetric Convective Model version 2 (ACM2, ref. [22]) PBL schemes. These four PBL schemes are the most widely used PBL schemes among the WRF model users. The YSU and ACM2 schemes are non-local schemes, and the MYJ and MYNN schemes are local schemes using a turbulence kinetic energy closure. In the four simulations, we used the surface-layer schemes relevant to the PBL schemes. We used the revised fifth-generation Pennsylvania State University–National Center for Atmospheric Research Mesoscale Model (MM5) surface-layer scheme for the YSU PBL scheme, the Eta similarity surface-layer scheme for the MYJ PBL scheme, the MYNN surface-layer scheme for the MYNN PBL scheme, and the Pleim-Xu surface-layer scheme for the ACM2 PBL scheme. For other physics schemes, we used the Dudhia shortwave radiation scheme [23], Rapid Radiative Transfer Model (RRTM) longwave radiation scheme [24], Kain–Fritsch cumulus convection scheme [25] only for the outermost two domains, and WRF single-moment 6-class cloud microphysics scheme [26] in the model. Additionally, we used a single-layer urban canopy model [27] to precisely reproduce urban meteorology. We integrated the model from 0300 LST on 16 January to 0300 LST on 19 January, and we used simulation data during the radiosonde observation period for the analysis.

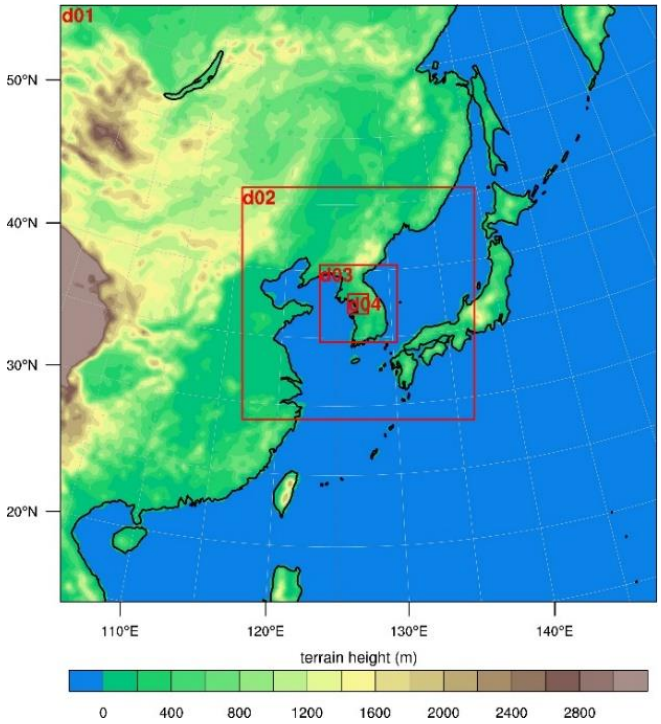

Figure 3. Domain configuration of the WRF model and terrain height.

4. Results

4.1. Observed Structures of Lower Troposphere

The Hovmöller diagrams of potential temperature, wind speed, wind direction, and water vapor mixing ratio from the radiosonde observation are shown in Figure 4 to illustrate temporal changes in the overall characteristics of the lower troposphere. From ~1900 LST on 17 January, the water vapor mixing ratio below 2 km from the ground abruptly increased and the dominant wind direction near the surface tended to change to westerly or northwesterly. These changes in water vapor mixing ratio and wind direction showed that the moisture advection by the westerly or northwesterly winds, illustrated in the synoptic weather patterns in Figure 1b,d, began to affect Seoul at ~1900 LST on 17 January. Because the moisture advection also caused cloudy weather in Seoul, the magnitude of the diurnal variation of the near-surface air temperature on 18 January was smaller than that on 17 January. From 0000 LST on 18 January, wind speed above a height of 1.2 km considerably increased. The strengthened air flow in the upper troposphere was related to the increase in wind speed above a height of 1.2 km.

To investigate the changes in the lower troposphere structure in detail, the vertical profiles of potential temperature and water vapor mixing ratio are shown in Figure 5. From 1000 LST to 1200 LST on 17 January, the potential temperature near the surface gradually increased, and the layer with a nearly constant potential temperature, i.e., the CBL, developed (Figure 5a). At 1300 LST on 17 January, the height of the CBL abruptly increased compared with that at 1200 LST on 17 January. A residual layer with a small vertical temperature gradient at a height of 0.3–0.9 km, appearing in the morning of January 17th, became a part of the CBL from 1200 LST to 1300 LST on 17 January. The abrupt increase in the CBL height was also previously observed [11]. At 1500 LST on 17 January, the CBL further developed. These characteristics of the CBL development are also reflected in the vertical profiles of water vapor mixing ratio in Figure 5b. Below 1 km, the water vapor mixing ratio, which generally decreased with height at 1200 LST, abruptly became almost constant at 1300 LST, implying a conversion process from the residual layer to the CBL.

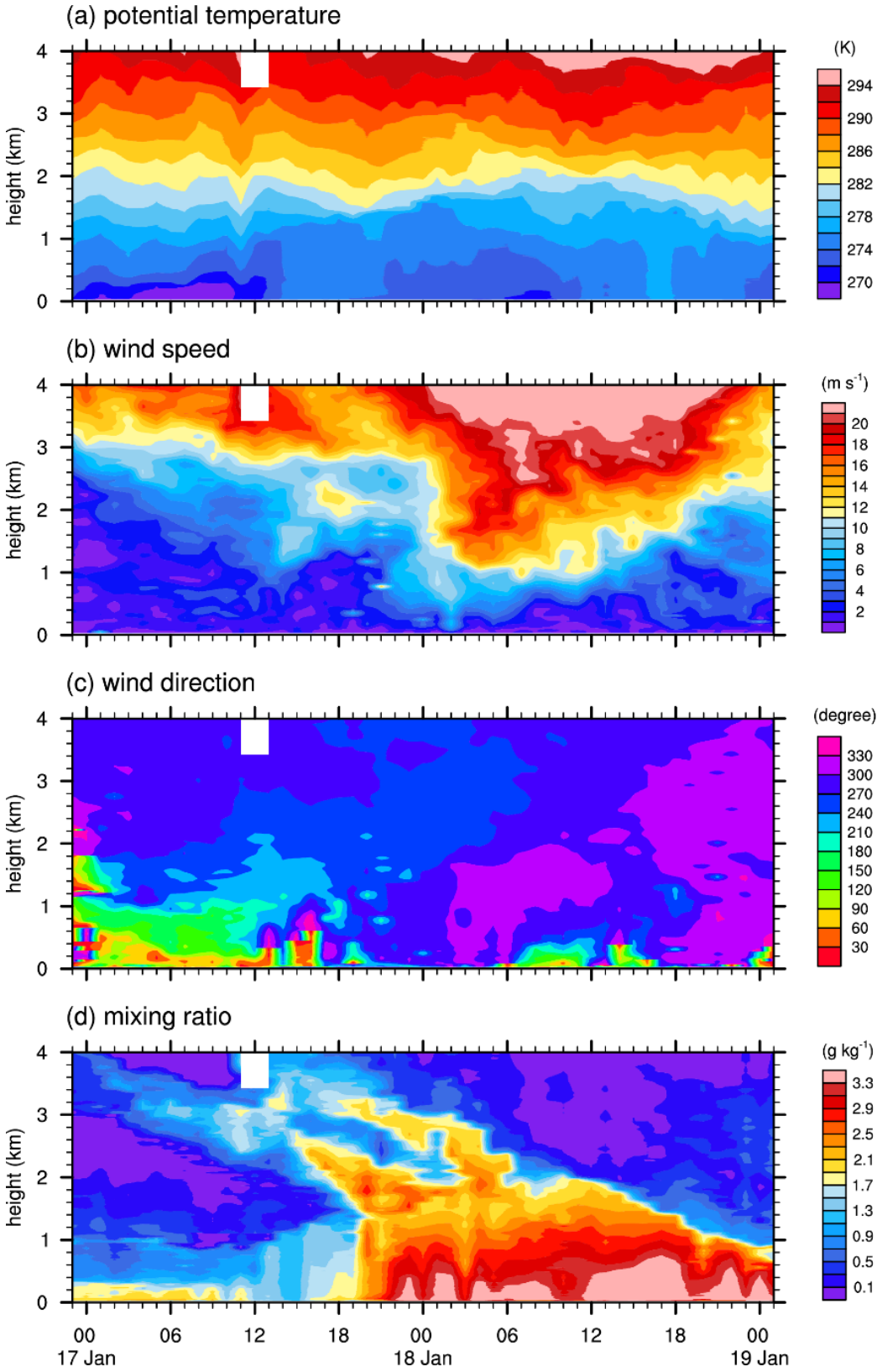

Figure 4. Hovmöller diagrams of (**a**) potential temperature, (**b**) wind speed, (**c**) wind direction, and (**d**) water vapor mixing ratio.

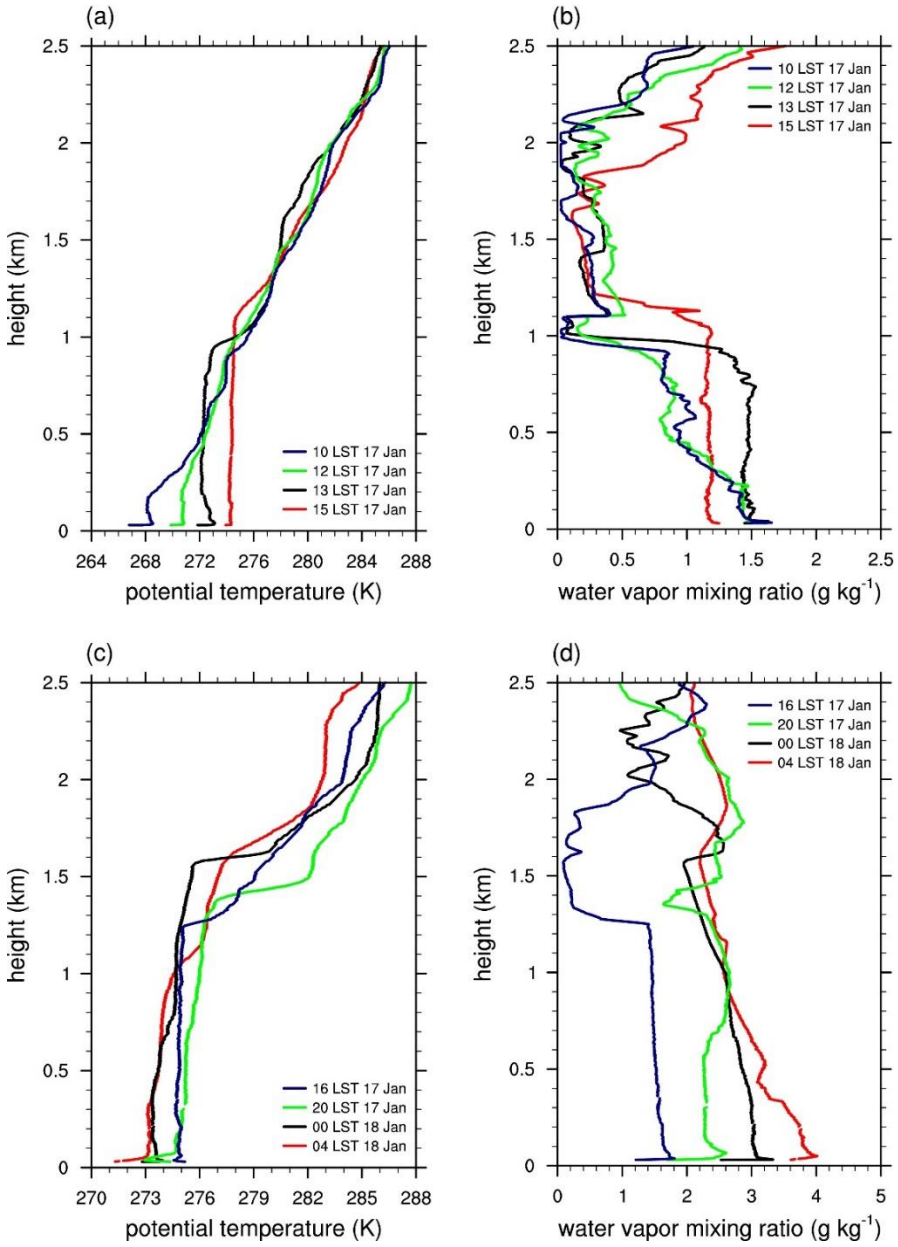

Figure 5. Vertical profiles of the (**a**,**c**) potential temperature and (**b**,**d**) water vapor mixing ratio at (**a**,**b**) 1000, 1200, 1300, and 1500 LST on 17 January 2017, and (**c**,**d**) 1600 and 2000 LST on 17 January 2017 and 0000 and 0400 LST on 18 January 2017.

From 1600 LST on 17 January to 0400 LST on 18 January, the cloudy weather induced by the moisture advection weakened radiative cooling and decreased potential temperature in the lower troposphere (Figure 5c). Additionally, the thick layer with small vertical temperature gradient was generally maintained. The vertical profiles of the water vapor mixing ratio more directly exhibit the effects of the moisture advection. At 2000 LST on 17 January, the water vapor mixing ratio below 2.2 km increased compared with that at 1600 LST on 17 January because the lower-level moisture advection began to affect the lower troposphere at ~1900 LST on 17 January (Figure 5d). Additionally, we observed the negative vertical gradient of water vapor mixing ratio in the lower troposphere after 2000 LST on 17 January. This negative vertical gradient of water vapor mixing ratio in the lower troposphere was still maintained until the daytime on 18 January, implying that water vapor was not well-mixed in the lower troposphere on 18 January because the radiative heating was weak under the cloudy weather.

4.2. Simulations

We validated the simulations with the YSU, MYJ, MYNN, and ACM2 PBL schemes using the radiosonde observation data and the ground meteorological data from Gangnam AWS (Figure 2). We show the simulated and observed 2-m air temperature and 10-m wind speed at the location of Gangnam AWS (Figure 6a,b). We also show the air temperatures and wind speeds from the numerical simulations and radiosonde observation at 925 and 850 hPa (Figure 6c–f). The WRF model overestimated the daily minimum air temperature on 17 January, but the diurnal variation of the observed 2-m air temperature was well-reproduced in all four simulations in general. Especially, in the four simulations, the air temperature decrease from 0000 to 0600 LST on 18 January was small due to the weakened radiative cooling by the cloudy weather, as exhibited in the observation. After 1800 LST on 18 January, the four simulations underestimated 2-m air temperature. The haze at the night on 18 January was not well-reproduced in the four simulations, resulting in an overestimation of radiative cooling from 1800 LST 18 January. The simulated 10-m wind speed was generally larger than the observed one. The magnitude of the 10-m wind speed increase from 1000 LST on 18 January was larger in the four simulations than in the observations. The wind speed decrease in urban areas due to buildings was not well-represented in the numerical simulations, similar to other numerical simulations [28–30]. At 925 and 850 hPa, the general tendencies of the simulated air temperatures in the four simulations reproduced those in the radiosonde observation. However, small-scale perturbations in the air temperature observation were not captured by the simulations in general. The general tendencies of the simulated 925 and 850 hPa wind speeds in the four simulations were similar to the observations, except for the wind speed increase from 0000 to 0600 LST on 18 January. The air flow in the upper troposphere related to the wind speed increase (Figure 4b) was not accurately reproduced in the simulations.

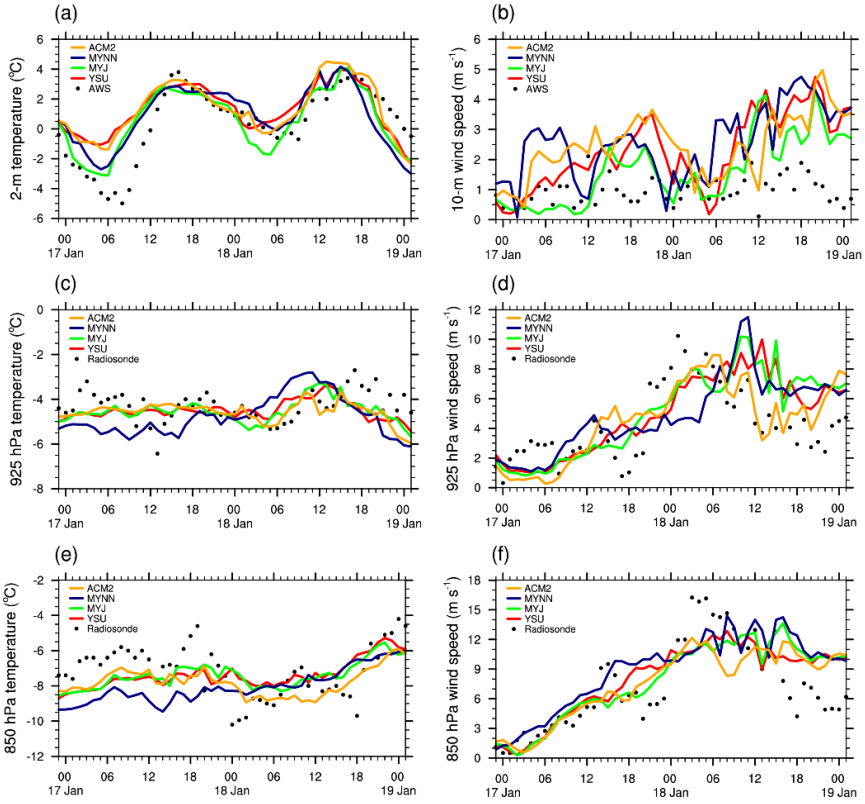

Figure 6. Time series of simulated and observed (**a**) 2-m air temperature and (**b**) 10-m wind speed at Gangnam AWS; (**c**) air temperature and (**d**) wind speed at 925 hPa, and (**e**) air temperature and (**f**) wind speed at 850 hPa.

Table 1 shows the mean bias error (MBE) and root mean square error (RMSE) of the simulated air temperature and wind speed near the surface at 925 and 850 hPa. Near the surface, the MBE and RMSE of the air temperature and wind speed were the smallest in the simulation with the MYJ scheme [31]. At 925 hPa, the MBE and RMSE of the air temperature were the smallest in the simulations with the YSU and MYJ schemes, respectively. The MBE and RMSE of the wind speed at 925 hPa were smallest in the simulation with the ACM2 scheme. At 850 hPa, the MBE and RMSE of the air temperature were the smallest in the simulations with the YSU and ACM2 schemes, respectively. For the 850 hPa wind speed, the simulations with the ACM2 and YSU schemes had the smallest MBE and RMSE, respectively. The MYJ scheme reproduced the second most accurate air temperature and wind speed at 850 hPa. By comparing the MBE and RMSE of the air temperature and wind speed, we concluded that the MYJ scheme reproduced the most accurate simulation results.

Table 1. Mean bias error (MBE) and root mean square error (RMSE) of the simulated 2-m, 925 hPa, and 850 hPa air temperature and 10-m, 925 hPa, and 850 hPa wind speed.

	MBE				**RMSE**			
	YSU	**MYJ**	**MYNN**	**ACM2**	**YSU**	**MYJ**	**MYNN**	**ACM2**
2-m air temperature (°C)	−0.93	−0.20	−0.53	−0.96	1.88	1.48	1.64	1.84
10-m wind speed (m s^{-1})	−1.38	−0.69	−1.62	−1.55	1.80	1.30	1.98	1.85
925 hPa air temperature (°C)	0.20	0.24	0.47	0.28	0.80	0.76	1.19	0.78
925 hPa wind speed (m s^{-1})	−0.65	−0.74	−0.62	−0.27	2.34	2.45	2.64	1.90
850 hPa air temperature (°C)	0.22	0.25	0.86	0.62	1.41	1.35	1.82	1.24
850 hPa wind speed (m s^{-1})	−0.58	−0.49	−1.53	−0.18	2.79	2.92	3.31	2.98

To compare the structures of the lower troposphere in the four simulations, Hovmöller diagrams of the potential temperature and water vapor mixing ratio using the simulation data at the location of the radiosonde launch site are shown in Figure 7. From 0800 to 1300 LST on 17 January, the potential temperature below ~1 km slowly increased in the four simulations compared with that in the observations. The four simulations did not reproduce the abrupt development of the layer with nearly constant potential temperature at 1300 LST. The process of the residual layer with a small vertical temperature gradient becoming a part of the CBL was not well-simulated in the four simulations. The smaller potential temperature variation below ~1 km on 18 January was well-reproduced in the four simulations, except for the large decrease in the potential temperature from ~1800 LST on 18 January. The simulation with the MYNN scheme showed the rapid increase in the potential temperature below ~1 km compared with the other simulations. Additionally, the height of the layer with a nearly constant potential temperature was the highest in the MYNN scheme (~1 km) and similar to that in the observation. Thus, we considered the MYNN scheme as the most accurate scheme in simulating the CBL development during the daytime on 17 January. This result is in line with that of another optimization study of WRF physical parameterization schemes [32].

At the initial stage of moisture advection on 17 January, the simulated water vapor mixing ratio near the surface was generally smaller than that at the upper level (height of ~1 km), whereas the observed water vapor mixing ratio was the largest near the surface. This implied that the advected moist air was not well-mixed with the pre-existing air near the surface in the simulations. The small-scale turbulences that play a large role in the mixing of air were not accurately reproduced by the PBL schemes in the study. Additionally, the amount of the advected moisture in the four simulations was generally less than that in the observation. From ~1800 LST on 18 January, the simulated water vapor mixing ratio below ~1 km decreased with time in general. We found that the simulated moisture advection ended earlier than the observed one, as shown in the 2-m air temperature time series. The simulation with the MYNN scheme showed the strongest moisture advection among the four simulations. Due to the strongest moisture advection and highest CBL

height, the water vapor mixing ratio increased above 2 km, similar to the observation. Therefore, we concluded that the simulation with the MYNN scheme performed the best in simulating the moisture advection from ~1900 LST on 17 January.

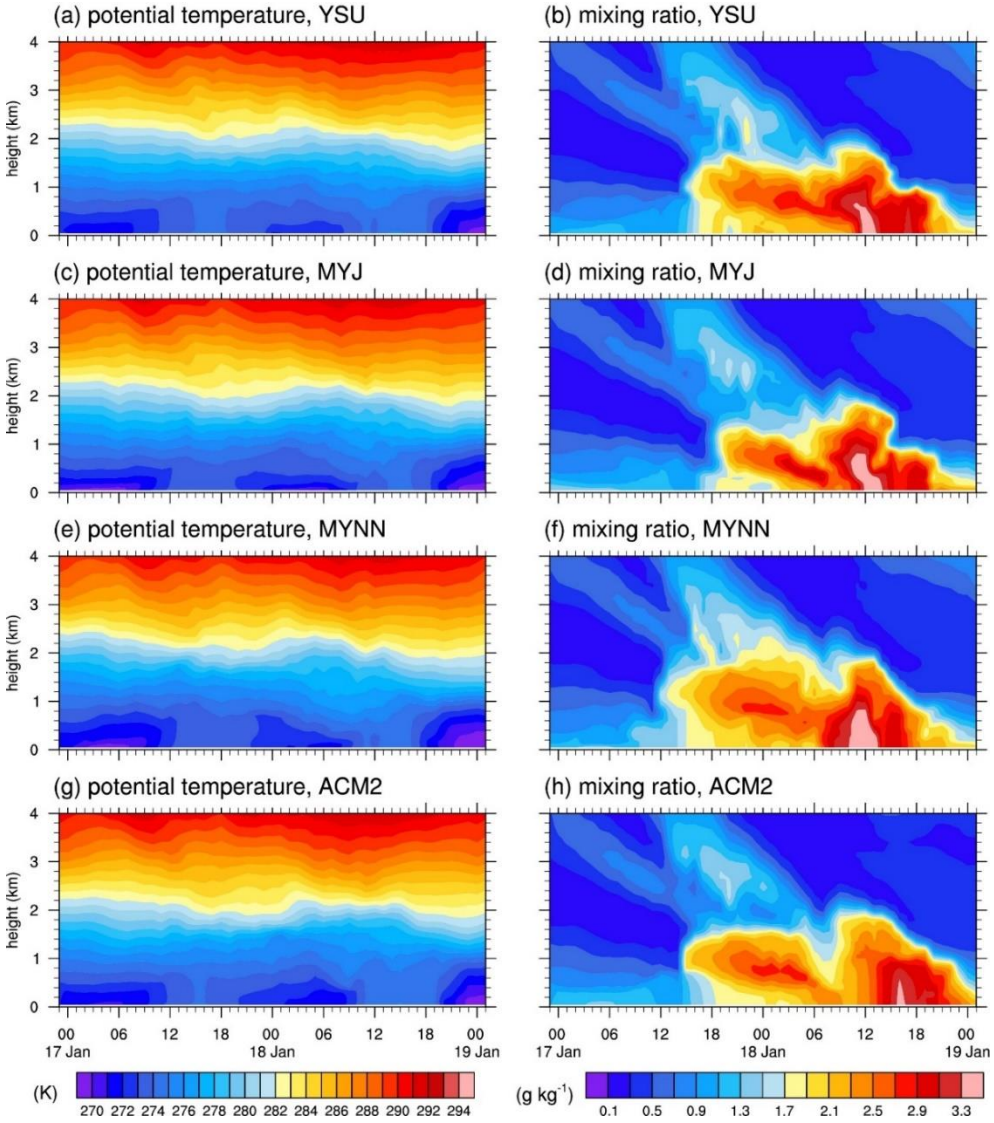

Figure 7. Hovmöller diagrams of potential temperature in simulations with (**a**) YSU, (**c**) MYJ, (**e**) MYNN, and (**g**) ACM2 PBL parameterization schemes; the water vapor mixing ratio in the simulations with (**b**) YSU, (**d**) MYJ, (**f**) MYNN, and (**h**) ACM2 PBL parameterization schemes.

To demonstrate the structures of the lower troposphere in the four simulations in detail, the vertical profiles of the simulated and observed potential temperature are shown in Figure 8. From 1000 to 1500 LST on 17 January, the CBL developed from the initial to the mature stage (Figure 8a,b). At the initial stage, the CBL height in the observations (~0.2 km) was similar to those in the simulations with the MYJ and MYNN schemes, and smaller than those in the simulation with the YSU and ACM2 schemes. At the mature stage, the CBL developed up to ~1.1 km. The CBL heights of the four simulations were smaller than the observed value; the simulation with the MYNN scheme showed the highest CBL height (~0.9 km), which was the closest to the observed CBL height. These simulation results showed that the development of the CBL height was the best described in the simulation with the MYNN scheme.

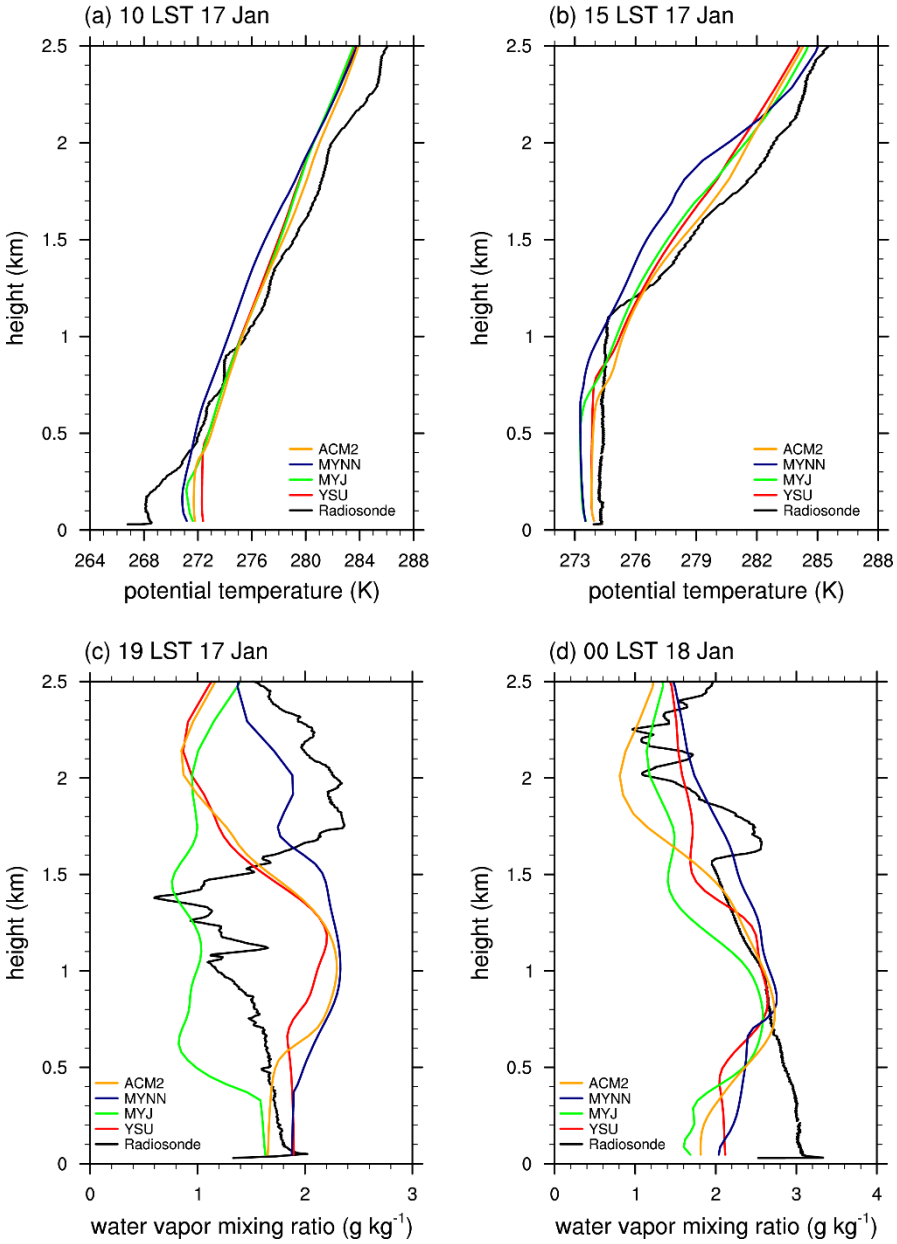

Figure 8. Vertical profiles of simulated and observed potential temperature at (**a**) 1000 and (**b**) 1500 LST on 17 January and water vapor mixing ratio at (**c**) 1900 LST on 17 January and (**d**) 0000 LST on 18 January.

At 1900 LST on 17 January, the moisture advection was in the initial stage (Figures 4d and 8c). Except for the simulation with the MYJ scheme, the simulated moisture advections appeared earlier than in the observations, which increased the water vapor mixing ratio at ~0.5 to ~2.0 km. Below 2.0 km, the simulation with the MYNN scheme showed a larger water vapor mixing ratio in general compared with the other simulations. At 0000 LST on 18 January, the moisture advection increased the water vapor mixing ratio below 2.0 km in general, and those in the four simulations also generally increased. The water vapor mixing ratios below 1.3 km in the four simulations were similar to each other, but at 1.3–2.0 km, the water vapor mixing ratio in the simulation with the MYNN scheme was still larger than that in the other simulations. The observed average water vapor mixing ratio below 2.0 km (2.8 g kg^{-1}) was larger than in the four simulations. The simulation with the MYNN scheme produced the largest average water vapor mixing ratio (2.3 g kg^{-1}) among the simulations (2.1, 1.9, and 2.0 g kg^{-1} for the simulations with the YSU, MYJ, and ACM2

schemes, respectively). These simulation results showed that the moisture advection in the simulation with the MYNN scheme produced a larger water vapor mixing ratio below 2.0 km, which was the closest to that in the radiosonde observations.

5. Summary and Conclusions

We performed 1 h interval radiosonde observations in a central urban area in Seoul, South Korea, to investigate the structures of the wintertime lower troposphere on 17 and 18 January 2017. On 17 January, a CBL with nearly constant potential temperature and water vapor mixing ratio gradually developed in the morning and then abruptly grew within 1 h starting from noon by merging the residual layer. From the afternoon on 17 January, moisture advection with clouds affected the lower troposphere, resulting in the weakening of radiative heating/cooling. Thus, in the lower troposphere, the temperature variation became small, and the layer with the small vertical temperature gradient was maintained on 18 January. The water vapor mixing ratio near the surface increased, and the negative vertical gradient of water vapor mixing ratio in the lower troposphere was maintained on 18 January. These maintained vertical structures of temperature and water vapor mixing ratio implied that the mixing in the lower troposphere weakened. We also investigated the performance of WRF models with the YSU, MYJ, MYNN, and ACM2 PBL parameterization schemes in simulating the structures of the lower troposphere. The overall trends in the air temperature and wind speed in the lower troposphere were generally reproduced well in the four simulations. However, the abrupt development of the layer with nearly constant potential temperature did not appear in the four simulations. The wind speed increase due to air flow in the upper troposphere was also not reproduced well in the simulations. The simulation with the MYJ scheme was the most accurate in reproducing the air temperature and wind speed in the lower troposphere compared with the other schemes. The simulated moisture advection was weaker and decayed earlier than the observed moisture advection. Additionally, the simulated water vapor mixing ratio near the surface was smaller than that at the upper level (~1 km) because the advected moist air was not well-mixed with the pre-existing air near the surface. Small-scale turbulence, which plays a role in mixing air, was not well-reproduced in the four simulations. Among the four schemes investigated, the MYNN scheme performed the best in simulating the CBL development and moisture advection in the observation period.

In this study, we found that the changes in the structures of the lower troposphere can quickly occur and be affected by small-scale turbulence. The WRF model with various PBL parameterization schemes does not capture the abrupt changes and mixing of air by small-scale turbulence in the lower troposphere. This is a case study with an entire time span of 2 days to keep a launching interval of 1 h, which is a limitation of this study. Further studies with high-resolution large-eddy simulation (LES) modeling are needed to accurately simulate the structure of the lower troposphere and improve the PBL scheme for multiple cases.

Author Contributions: Conceptualization, B.-S.H. and J.-H.H.; formal analysis, B.-S.H.; validation, B.-S.H.; investigation, B.-S.H. and J.-H.H.; data curation, B.-S.H.; writing—original draft preparation, B.-S.H.; writing—review and editing, B.-S.H., K.-H.K. and S.-B.P.; visualization, B.-S.H.; supervision, K.-H.K. All authors have read and agreed to the published version of the manuscript.

Funding: This work was funded by the Research Institute of Basic Sciences funded by the National Research Foundation of Korea (NRF-2019R1A6A1A10073437) and funded by the Ministry of Science and ICT (NRF-2020R1C1C1012354).

Institutional Review Board Statement: Not applicable.

Informed Consent Statement: Not applicable.

Data Availability Statement: The weather maps and meteorological observation data are available from https://data.kma.go.kr on demand (accessed on 31 March 2017).

Acknowledgments: The authors would thank the Korea Meteorological Administration for providing the weather maps and meteorological observation data.

Conflicts of Interest: The authors declare no conflict of interest. The funders had no role in the design of the study; in the collection, analyses, or interpretation of data; in the writing of the manuscript; or in the decision to publish the results.

References

1. Lothon, M.; Campistron, B.; Jacoby-Koaly, S.; Bénech, B.; Lohou, F.; Girard-Ardhuin, F. Comparison of radar reflectivity and vertical velocity observed with a scannable C-band radar and two UHF profilers in the lower troposphere. *J. Atmos. Oceanic Technol.* **2002**, *19*, 899–910. [CrossRef]
2. Zhang, C.; Woodworth, P.; Gu, G. The seasonal cycle in the lower troposphere over West Africa from sounding observations. *Q. J. R. Meteorol. Soc.* **2006**, *132*, 2559–2582. [CrossRef]
3. Martucci, G.; Matthey, R.; Mitev, V.; Richner, H. Comparison between backscatter lidar and radiosonde measurements of the diurnal and nocturnal stratification in the lower troposphere. *J. Atmos. Ocean. Technol.* **2007**, *24*, 1231–1244. [CrossRef]
4. Song, H.-J.; Kim, S.; Lee, H.; Kim, K.-H. Climatology of tropospheric relative humidity over the Korean Peninsula from radiosonde and ECMWF reanalysis. *Atmosphere* **2020**, *11*, 704. [CrossRef]
5. Mason, P.J. Large-eddy simulation of the convective atmospheric boundary layer. *J. Atmos. Sci.* **1989**, *46*, 1492–1516. [CrossRef]
6. Park, S.-B.; Baik, J.-J. Large-eddy simulations of convective boundary layers over flat and urbanlike surfaces. *J. Atmos. Sci.* **2014**, *71*, 1880–1892. [CrossRef]
7. Zhou, B.; Chow, F.K. Nested large-eddy simulations of the intermittently turbulent stable atmospheric boundary layer over real terrain. *J. Atmos. Sci.* **2014**, *71*, 1021–1039. [CrossRef]
8. Park, S.-B.; Baik, J.-J. Characteristics of decaying convective boundary layers revealed by large-eddy simulations. *Atmosphere* **2020**, *11*, 434. [CrossRef]
9. Cooper, D.; Eichinger, W. Structure of the atmosphere in an urban planetary boundary layer from lidar and radiosonde observations. *J. Geophys. Res.* **1994**, *992*, 22937–22948. [CrossRef]
10. Bianco, L.; Djalalova, I.V.; King, C.W.; Wilczak, J.M. Diurnal evolution and annual variability of boundary-layer height and its correlation to other meteorological variables in California's Central Valley. *Bound.-Layer Meteorol.* **2011**, *140*, 491–511. [CrossRef]
11. Ao, Y.; Li, J.; Li, Z.; Lyu, S.; Jiang, C.; Wang, M. Relation between the atmospheric boundary layer and impact factors under severe surface thermal conditions. *Adv. Meteorol.* **2017**, *2017*, 8352461. [CrossRef]
12. Deardorff, J.W. Parameterization of the planetary boundary layer for use in general circulation models. *Mon. Weather Rev.* **1972**, *100*, 93–106. [CrossRef]
13. Suarez, M.J.; Arakawa, A.; Randall, D.A. The parameterization of the planetary boundary layer in the UCLA general circulation model: Formulation and results. *Mon. Weather Rev.* **1983**, *111*, 2224–2243. [CrossRef]
14. Hong, S.Y.; Pan, H.L. Nonlocal boundary layer vertical diffusion in a medium-range forecast model. *Mon. Weather Rev.* **1996**, *124*, 2322–2339. [CrossRef]
15. Gilliam, R.C.; Pleim, J.E. Performance assessment of new land surface and planetary boundary layer physics in the WRF-ARW. *J. Appl. Meteorol. Climatol.* **2010**, *49*, 760–774. [CrossRef]
16. Hariprasad, K.B.R.R.; Srinivas, C.V.; Singh, A.B.; Rao, S.V.B.; Baskaran, R.; Venkatraman, B. Numerical simulation and intercomparison of boundary layer structure with different PBL schemes in WRF using experimental observations at a tropical site. *Atmos. Res.* **2014**, *145–146*, 27–44. [CrossRef]
17. Tyagi, B.; Magliulo, V.; Finardi, S.; Gasbarra, D.; Carlucci, P.; Toscano, P.; Zaldei, A.; Riccio, A.; Calori, G.; D'Allura, A.; et al. Performance analysis of planetary boundary layer parameterization schemes in WRF modeling set up over Southern Italy. *Atmosphere* **2018**, *9*, 272. [CrossRef]
18. Skamarock, W.C.; Klemp, J.B.; Dudhia, J.; Gill, D.O.; Barker, D.M.; Duda, M.G.; Huang, X.-Y.; Wang, W.; Powers, J.G. *A Description of the Advanced Research WRF Version 3*; Mesoscale and Microscale Meteorology Division in National Center for Atmospheric Research: Boulder, CO, USA, 2008.
19. Hong, S.-Y.; Noh, Y.; Dudhia, J. A new vertical diffusion package with an explicit treatment of entrainment processes. *Mon. Weather Rev.* **2006**, *134*, 2318–2341. [CrossRef]
20. Janjić, Z.I. The step-mountain eta coordinate model: Further developments of the convection, viscous sublayer, and turbulence closure schemes. *Mon. Weather Rev.* **1994**, *122*, 927–945. [CrossRef]
21. Nakanishi, M.; Niino, H. An improved Mellor–Yamada level 3 model: Its numerical stability and application to a regional prediction of advecting fog. *Bound.-Layer Meteorol.* **2006**, *119*, 397–407. [CrossRef]
22. Pleim, J.E. A Combined Local and Nonlocal Closure Model for the Atmospheric Boundary Layer. Part I: Model Description and Testing. *J. Appl. Meteor. Climatol.* **2007**, *46*, 1383–1395. [CrossRef]
23. Dudhia, J. Numerical study of convection observed during the Winter Monsoon Experiment using a mesoscale two-dimensional model. *J. Atmos. Sci.* **1989**, *46*, 3077–3107. [CrossRef]
24. Mlawer, E.J.; Taubman, S.J.; Brown, P.D.; Iacono, M.J.; Clough, S.A. Radiative transfer for inhomogeneous atmospheres: RRTM, a validated correlated-k model for the longwave. *J. Geophys. Res.* **1997**, *102*, 16663–16682. [CrossRef]

25. Kain, J.S. The Kain–Fritsch convective parameterization: An update. *J. Appl. Meteorol.* **2004**, *43*, 170–181. [CrossRef]
26. Hong, S.-Y.; Lim, J.-O.J. The WRF single-moment 6-class microphysics scheme (WSM6). *J. Korean Meteorol. Soc.* **2006**, *42*, 129–151.
27. Chen, F.; Kusaka, H.; Bornstain, R.; Ching, J.; Grimmond, C.S.B.; Grossman-Clarke, S.; Loridan, T.; Manning, K.; Martilli, A.; Miao, S.; et al. The integrated WRF/urban modeling system: Development, evaluation, and applications to urban environmental problems. *Int. J. Climatol.* **2011**, *31*, 273–288. [CrossRef]
28. Kim, D.-J.; Kang, G.; Kim, D.-Y.; Kim, J.-J. Characteristics of LDAPS-predicted surface wind speed and temperature at automated weather stations with different surrounding land cover and topography in Korea. *Atmosphere* **2020**, *11*, 1224. [CrossRef]
29. Zhang, L.; Xin, J.; Yin, Y.; Chang, W.; Xue, M.; Jia, D.; Ma, Y. Understanding the major impact of planetary boundary layer schemes on simulation of vertical wind structure. *Atmosphere* **2021**, *12*, 777. [CrossRef]
30. Jiang, L.; Bessagnet, B.; Meleux, F.; Tognet, F.; Couvidat, F. Impact of physics parameterizations on high-resolution air quality simulations over the Paris region. *Atmosphere* **2020**, *11*, 618. [CrossRef]
31. Lee, S.-H.; Kwak, K.-H. Assessing 3-D spatial extent of near-road air pollution around a signalized intersection using drone monitoring and WRF-CFD modeling. *Int. J. Environ. Res. Public Health* **2020**, *17*, 6915. [CrossRef]
32. Yoon, J.W.; Lim, S.; Park, S.K. Combinational optimization of the WRF physical parameterization schemes to improve numerical sea breeze prediction using micro-genetic algorithm. *Appl. Sci.* **2021**, *11*, 11221. [CrossRef]